Research Square

Preprints are preliminary reports that have not undergone peer review.
They should not be considered conclusive, used to inform clinical practice,
or referenced by the media as validated information.

Direct Resolution of Three-Dimensional Gaze for Spatial Interaction via a Smart Contact Lens

Tianling Ren

rentl@tsinghua.edu.cn

Tsinghua University https://orcid.org/0000-0002-7330-0544

Xinyuan Jia

Tsinghua University

Bingchen Zhao

School of Integrated Circuits, Tsinghua University Beijing National Research Center for Information Science and Technology (BNRist), Tsinghua University https://orcid.org/0009-0004-6543-3330

Jiaju Yin

School of Integrated Circuits, Tsinghua University Beijing National Research Center for Information Science and Technology (BNRist), Tsinghua University

Haorong Li

Tsinghua University

Jiong Pan

Tsinghua University https://orcid.org/0009-0009-2036-6492

Zi-Gan Xu

Tsinghua University

Zeda Wang

Tsinghua University

Lu-Qi Tao

Institute of Microelectronics & Beijing National Research Center for Information Science and Technology and Department of Electronic Engineering, Tsinghua University

Yi Yang

Tsinghua University

Article

Keywords:

Posted Date: April 10th, 2026

DOI: https://doi.org/10.21203/rs.3.rs-9214452/v1

License: This work is licensed under a Creative Commons Attribution 4.0 International License.
Read Full License

Additional Declarations: There is **NO** Competing Interest.

Direct Resolution of Three-Dimensional Gaze for Spatial Interaction via a Smart Contact Lens

Xinyuan Jia[1,2], Binchen Zhao[3], Jiaju Yin[1,2], Haorong Li[4], Jiong Pan[1,2], Zigan Xu[1,2], Zeda Wang[1,2], Lu-Qi Tao[2,*], Yi Yang[1,2,*] and Tian-Ling Ren[1,2,*].

[1]School of Integrated Circuits, Tsinghua University, Beijing 100084, China.
[2]Beijing National Research Center for Information Science and Technology (BNRist), Tsinghua University, Beijing 100084, China.
[3]School of Integrated Circuits, Peking University, Beijing 100871, China.
[4]Weiyang College, Tsinghua University, Beijing 100084, China.
* Corresponding author. RenTL@tsinghua.edu.cn, yiyang@tsinghua.edu.cn, taoluqi@tsinghua.edu.cn

Abstract:

As eye-machine interaction (EMI) systems evolve towards more immersive and spatially distributed environments, a key challenge lies in reliably capturing and utilizing fixation depth for precise interaction in real-world settings. However, existing eye-tracking technologies estimate fixation depth indirectly through geometric reconstruction or binocular triangulation, limiting robustness and wearable deployment in spatial environments. Here we present Embobi, a non-invasive, wireless, and chipless smart contact lens that enables direct resolution of three-dimensional gaze at the ocular interface. By transducing accommodation-induced corneal deformation into resonance-frequency shifts of an integrated inductive coil array, the system jointly captures gaze direction and fixation depth without reliance on scene cameras or dual-eye triangulation. Dedicated gaze decoding and edge-level inference algorithms structurally decouple depth and direction at the sensing node, enabling stable reconstruction of three-dimensional points of regard. Validation across eye phantoms, ex vivo porcine eyes, and in vivo rabbit models demonstrates gaze-direction accuracy comparable to commercial eye trackers alongside repeatable depth sensing. Representative interaction scenarios illustrate that physiologically resolved fixation states can function as continuous control variables, enabling spatially anchored eye–machine interaction. This work establishes a pathway toward physiology-grounded on-eye interfaces in which perceptual states can serve more directly as interaction signals.

Introduction

With the rapid advancements in artificial intelligence (AI), extended reality (XR), and the development of embodied intelligence technologies, eye-machine interaction (EMI) has gained increasing attention as a more intuitive, non-contact method of interaction. Companies like Apple, Meta, and Google have launched smart eyewear products, such as the Meta Ray-Ban Stories and Apple Vision Pro, incorporating features like eye-tracking, gesture control, and AI-powered assistants. However, many current EMI devices remain centered on two-dimensional, screen-based interaction, offer only limited interactive functionality, or depend on bulky and conspicuous head-mounted hardware[1–3]. As EMI expands toward immersive, assistive, and spatially distributed intelligent environments[4–7], existing systems increasingly struggle to achieve stable and reliable performance in real-world settings. In such environments, multiple objects often align along similar viewing directions while differing in depth, rendering gaze direction alone inadequate for reliably identifying the intended target of interaction[8–10]. Consequently, accurate access to fixation depth has become a prerequisite for next-generation EMI, rather than an optional enhancement[10,11]

A common limitation shared by prevailing gaze-tracking approaches is that fixation depth is not sensed directly, but inferred through backend computation[8,12,13]. Most existing methods rely on binocular triangulation[14,15], geometric reconstruction[16,17], statistical inference[8,18], or environmental context[19,20] to estimate depth as a derived variable, rather than accessing it at the perceptual source. As a result, depth estimation is highly sensitive to measurement noise, user motion, and calibration drift, with errors that accumulate and amplify as viewing distance increases[21–24]. Moreover, these inference-based frameworks offer limited interpretability and robustness in natural scenes[8,25,26], where visual attention is often distributed across extended objects or regions rather than well-defined point targets. To compensate, some systems incorporate scene cameras or environmental modeling, further increasing computational load, energy consumption, and system complexity[27,28]. Together, these constraints have confined most practical eye-tracking systems to two-dimensional operation[24,29], where depth ambiguity is avoided rather than resolved. More fundamentally, existing approaches treat fixation depth as an inferred variable based on external geometry, rather than as a physiological quantity generated by the visual system itself [21,30,31].

Human perception is inherently embodied: key perceptual variables are resolved within the sensing organ itself rather than reconstructed through extensive downstream computation. Visual attention follows this principle, with both the direction and depth of gaze encoded through intrinsic physiological processes of the eye[32–34]. Rather than relying on external geometry or environmental reconstruction to infer visual attention, an alternative paradigm is to treat gaze sensing as an embodied process rooted in the intrinsic physiology of the eye. Human fixation is governed not only by ocular rotation but also by ocular accommodation, during which the eye dynamically adjusts its optical state to establish focus at different depths[35–37]. Importantly, accommodation is accompanied by continuous and reversible biomechanical responses of the anterior eye[38,39], including subtle yet systematic deformations at the corneal surface[40–45]. Within the physiological range of natural vision, these accommodation-induced corneal responses evolve monotonically with focal distance, are tightly time-locked to fixation behavior, and remain largely invariant to gaze direction and environmental context[40,46]. This combination of monotonicity, reversibility, and task-specific coupling distinguishes accommodation-related corneal deformation from other ocular signals and renders it uniquely suitable as a direct physiological proxy for fixation depth. By incorporating this accommodation-related dimension, fixation depth is encoded at the physiological level and captured in situ, eliminating the need for extensive backend computation and aligning eye–machine interaction with the organizational principles of human perception.

Accessing this embodied physiological channel requires a sensing interface that is mechanically coupled to the eye while remaining optically transparent, lightweight, and behaviorally unobtrusive. A smart contact lens naturally satisfies these requirements[47,48]. By conformally interfacing with the corneal surface, a contact lens is inherently positioned to transduce accommodation-related biomechanical changes while preserving natural vision and eye movements[49,50].Crucially, the mechanical conformity between the lens and the cornea enables accommodation-induced deformation to be resolved with sufficient sensitivity and stability, making the on-eye interface a compelling route for direct depth sensing.

To operationalize this embodied sensing paradigm, we present Embobi, a non-invasive, wireless, and chipless smart contact lens system that enables direct reconstruction of three-dimensional points of regard in real-world environments. Using RLC resonance-based spectral analysis, the system simultaneously captures gaze direction and accommodation-related depth information for accurate three-dimensional gaze estimation without reliance on traditional dual-eye triangulation or scene cameras. We integrate a miniaturized inductive coil array into a soft smart contact lens with geometry optimized for ocular anatomy and develop dedicated signal-processing algorithms for independent extraction of gaze direction and fixation depth. System performance is validated across hydrogel-lens eye phantoms, mechanical eye-movement platforms, ex vivo porcine eyes, and in vivo rabbit models, demonstrating gaze-direction accuracy comparable to commercial eye trackers alongside stable and repeatable depth sensing. Representative eye–machine interaction scenarios, including ocular input, virtual-reality gaze interaction, and real-world wheelchair navigation, further illustrate the practical relevance of physiologically grounded, in-body gaze sensing. Together, these results establish a smart contact lens–based approach for direct resolution of three-dimensional gaze in real-world environments, enabling interaction to be guided more directly by perceptual states and laying the foundation for spatial interaction beyond screen-based paradigms.

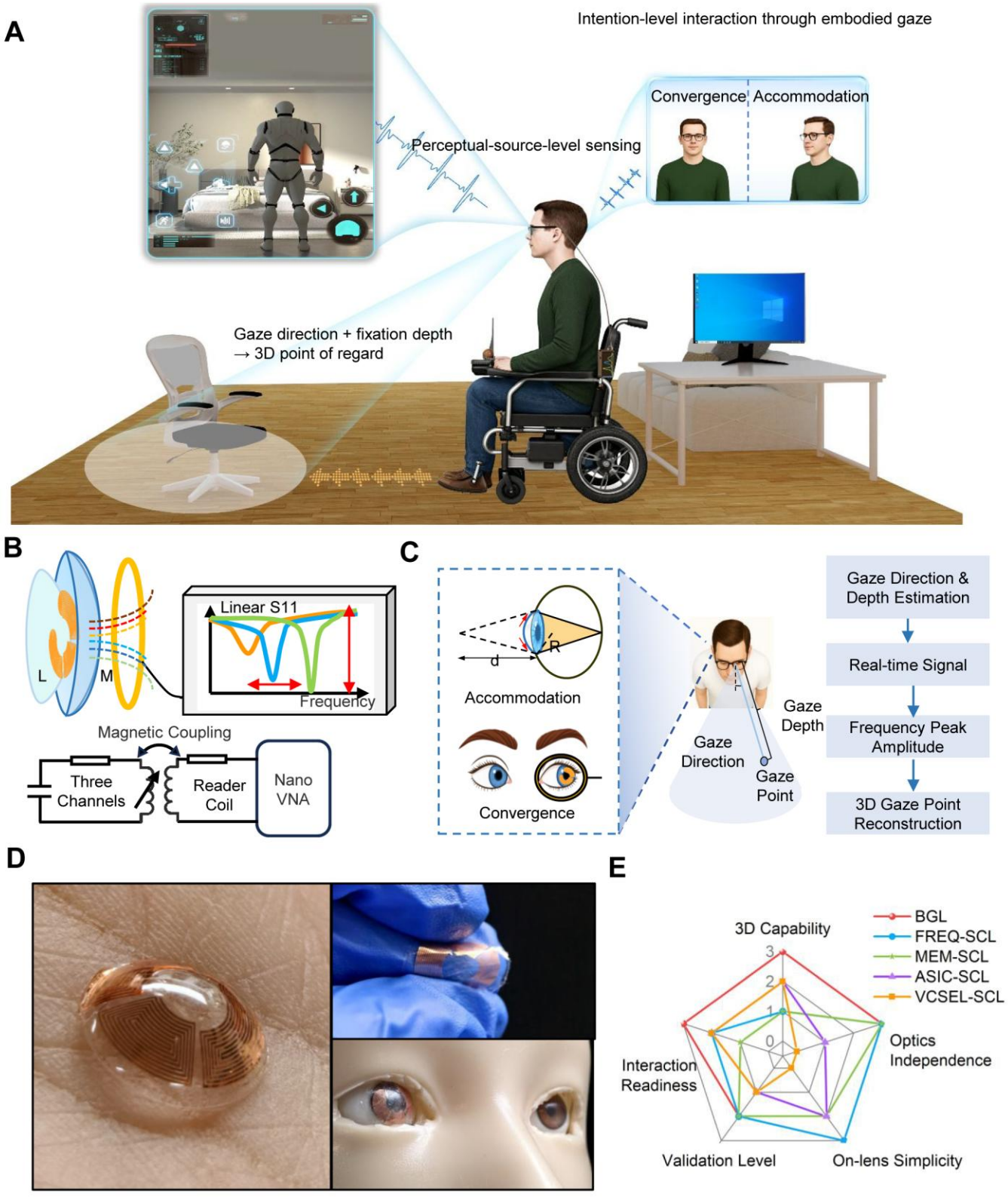


Fig. 1: Conceptual framework and system overview of Embobi.
(A) Application scenarios of Embobi, including gaze-based text input, virtual-reality interaction, and target-driven wheelchair navigation. **(B)** Wireless mutual-coupling sensing scheme integrating three embedded resonant coils and an external reader coil. Frequency shifts encode corneal-curvature variation (depth proxy), while resonance-peak amplitude modulation encodes gaze direction. **(C)** Physiological basis of three-dimensional gaze

reconstruction through accommodation-derived depth sensing and direction fusion. **(D)** Photographs of Embobi under normal, stretched, and bent conditions, demonstrating mechanical compliance. **(E)** Functional comparison of Embobi with representative smart contact lens technologies in terms of three-dimensional capability, optical independence, and interaction readiness.

Design concept and sensing principle of Embobi

Figure 1A illustrates the conceptual framework and application scope of Embobi, a three-dimensional gaze-sensing smart contact lens that integrates dual-modal physiological encoding of gaze direction and corneal curvature. By structuring gaze as a spatial coordinate rather than a two-dimensional projection, Embobi establishes a perception-driven interaction pathway, offering a lightweight and inconspicuous option for daily interaction, particularly for individuals with aphasia, anarthria, or severe motor impairments.

In communication scenarios, gaze-based trajectory writing enables character-level input, while integration with a nine-key framework allows word-level entry. In mobility-assistance scenarios, corneal-curvature monitoring provides access to fixation-depth information, which can be combined with gaze-direction signals for target-driven spatial interaction. In immersive environments such as virtual reality (VR), real-time gaze-direction sensing supports intuitive viewpoint control.

As shown in Fig. 1B, Embobi operates through a passive wireless electromagnetic mutual-coupling scheme. Three inductive resonant channels (Ch1–Ch3) with distinct resonance frequencies are embedded within the flexible contact lens, and an external reader coil integrated into eyeglass frames enables non-contact excitation and spectral interrogation. During natural fixation, accommodation is accompanied by subtle but reproducible corneal-curvature changes, which provide an accessible on-eye proxy for fixation depth (Supplementary Fig. 1 and Supplementary Table 1). In the present system, deformation at the lens–cornea interface perturbs the effective inductance and capacitance of each resonant channel, whereas ocular rotation primarily modulates the coupling strength between the reader coil and each channel, producing channel-dependent changes in resonance-peak amplitude.

For an individual resonant channel, the resonance frequency is given in first order by

$$f_i \approx \frac{1}{2\pi\sqrt{L_i C_i}} \tag{1}$$

and, under small curvature deformation, varies approximately linearly with the corneal radius of curvature r :

$$\Delta f_i \propto \Delta r \tag{2}$$

Accordingly, the resonance-frequency shifts of the inductive array directly reflect accommodation-related corneal-curvature variation and can therefore serve as a proxy for fixation depth. This approximation follows the standard inductive-strain relationship established for curved spiral resonators under small deformation, and the full derivation is provided in Supplementary Note 1.

By contrast, gaze rotation changes the relative alignment between the reader coil and the embedded resonators, thereby modulating the resonance-peak amplitudes of Ch1–Ch3 in a channel-dependent manner. The amplitude response can therefore be represented as

$$A = [A_{Ch1}, A_{Ch2}, A_{Ch3}\,] \tag{3}$$

where the three-channel amplitude pattern encodes gaze direction. In this way, resonance-frequency shifts report accommodation-related depth variation, whereas the relative amplitude responses across Ch1–Ch3 report gaze direction, enabling simultaneous estimation of three-dimensional points of regard.

During natural vision, accommodation and convergence operate together to maintain clear retinal imaging across viewing distances. Unlike conventional binocular eye trackers that infer fixation points through geometric intersection of two gaze vectors, Embobi encodes depth information from physiological deformation of a single eye and combines it with direction signals to reconstruct three-dimensional points of regard (3D PoR) (Fig. 1C). Figure 1D presents photographs of the fabricated Embobi device and its placement on a human-eye mannequin, demonstrating the compact form factor and mechanical compliance required for contact-lens integration. The device maintains a low-profile structure compatible with corneal curvature while preserving optical transparency of the visual axis.

To position Embobi within the broader landscape of gaze-sensing technologies, we compared representative smart contact lens systems across key architectural dimensions (Fig. 1E; Table 1). Existing smart contact lens approaches predominantly focus on eye-motion detection or gaze-direction estimation and typically do not provide access to fixation depth[3,51–55]. Meanwhile, alternative approaches for depth-aware gaze sensing based on smart glasses or head-mounted displays usually rely on binocular triangulation or related geometric reconstruction methods. By contrast, Embobi integrates resonance-frequency-based depth decoding and resonance-peak-amplitude-based gaze-direction decoding within a single passive on-eye device, enabling three-dimensional point-of-regard estimation without cameras, scene modeling, or active electronics.

Table 1. Comparison of Embobi with representative smart contact lens–based eye tracking systems

Device / system	Primary output	Depth (fixation/gaze)	Sensing / tracking principle	On-lens electronics	Wireless / external dependency	Validation	Reported performance (key)	Typical limitations vs. Embobi
Embobi (this work)	**3D point of regard (direction + fixation depth)**	**Yes (fixation depth; near/intermediate/far)**	**Chipless RLC resonance sensing; corneal-curvature–modulated frequency (depth) + amplitude distribution (direction)**	**Chip-free, battery-free**	**Reader coil + spectral analysis (no optics)**	**Eye phantom + ex vivo porcine eye + in vivo rabbit**	**Angular accuracy <1°; stable fixation-depth discrimination**	—
SCL[3]	Eye movement + eye closure (direction)	No (not emphasized)	Chip-free RLC resonance frequency encoding	Chip-free, battery-free	Reader coil + algorithm	Eye model + in vivo rabbit	Angular accuracy < 0.5°	Depth not addressed; focuses on motion/closure rather than point of regard
Photodiode-Based Gaze Lens (PD-SCL)[51]	Gaze direction	No	On-lens photodiodes + eyewear IR illumination; barycenter of photocurrents	ASIC on lens	Inductive powering + eyewear illumination	Artificial eyeball (prototype)	~0.2° accuracy (layout-based)	Strong dependence on eyewear illumination and optical path
ASIC-Integrated Gaze & Blink Lens (ASIC-SCL)[55]	Gaze direction + blink patterns	No	Four IR photodiodes + centroid computation	ASIC on lens	Inductive power + NFC to eyewear	Mock-up eyeball + artificial eyelid	~0.2° angular accuracy	Requires optical illumination; contains active chip
VCSEL[52]	Gaze + target designation	No	On-lens VCSEL optical pointers	Active emitters	Requires eyewear/receiver system	Characterization + integration concept	NR	Active optical path; alignment and system-complexity constraints
Blink-Encoded EMI Lens (Blink-RLC-SCL)[53]	Blink-based control signals	No	RLC resonance modulation by mechanical deformation (blink encoding)	Chip-free, battery-free	Reader coil + decoding algorithm	Experimental validation	82% blink recognition	Encodes control gestures only; no gaze direction or depth
Magnetic Eye-Motion Lens (MEM-SCL)[54]	Eye movement monitoring (classification)	No	Magnetic eye-movement sensing + electromagnetic coupling	Integrated functional layers	Wireless aggregation to portable reader	Ex vivo + in vivo rabbit	Eye-movement recognition accuracy ≥ 97%	Not designed for fine gaze pointing or 3D point-of-regard

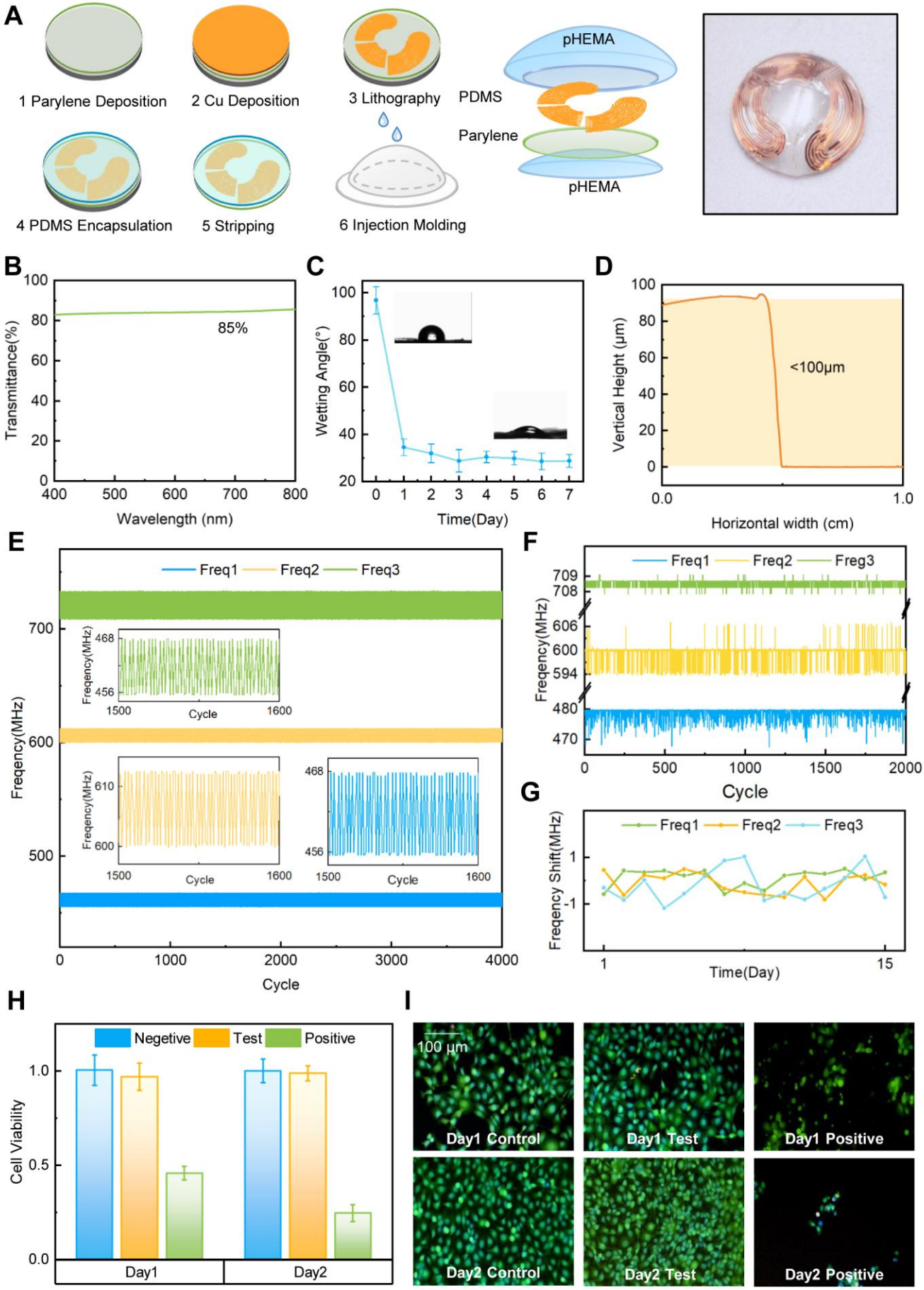

A
1 Parylene Deposition
2 Cu Deposition
3 Lithography
4 PDMS Encapsulation
5 Stripping
6 Injection Molding
pHEMA
PDMS
Parylene
pHEMA
B
Transmittance(%)
85%
Wavelength (nm)
C
Wetting Angle(°)
Time(Day)
D
Vertical Height (μm)
<100μm
Horizontal width (cm)
E
Freq1
Freq2
Freq3
Freqency(MHz)
Cycle
F
Freq1
Freq2
Freg3
Freqency(MHz)
Cycle
G
Freq1
Freq2
Freq3
Freqency Shift(MHz)
Time(Day)
H
Negetive
Test
Positive
Cell Viability
Day1
Day2
I
100 μm
Day1 Control
Day1 Test
Day1 Positive
Day2 Control
Day2 Test
Day2 Positive

Fig. 2: Characterization of the Sensing Interface of Embobi.

(A) Fabrication process of Embobi, with exploded-view schematic and optical image of the final device. **(B)** Visible-light transmittance of the central region of Embobi. **(C)** Water contact-angle measurements of Embobi surfaces before and after hydrophilic treatment (n = 5), with representative images. **(D)** Thickness profile of Embobi. **(E)** Stability of the baseline resonant frequency of Embobi under cyclic pressure loading, simulating repeated blinking during daily wear. **(F)** Stability of the baseline resonant frequency of Embobi under cyclic bending fatigue, mimicking routine lens handling and pick-up. **(G)** Stability of the baseline resonant frequency of Embobi in artificial tear fluid. **(H)** Cytotoxicity assessment of Embobi using human corneal epithelial cells (HCE-T), with cell viability quantified after 24 h and 48 h of incubation (n = 6). **(I)** Representative fluorescence images of HCE-T cells cultured with negative control medium, Embobi extracts, and positive control medium after 24 h and 48 h. Scale bar, 100 μm.

The Embobi integrates three coaxially aligned spiral inductors within a soft contact lens to enable simultaneous sensing of gaze direction and corneal curvature. The geometrical parameters of the inductors were carefully optimized such that the central 5-mm optical zone of the lens remains unobstructed, while three spatially separated and mutually noninterfering resonance peaks are preserved (Supplementary Fig. 2, 3). Compared with a single-inductor design, the distributed inductor configuration mitigates the influence of common-mode interference, such as temperature-induced frequency drift, on corneal-curvature measurements, and additionally facilitates robust extraction of gaze-direction information.

The inductors were fabricated using a photolithography–electroplating process on an ultrathin Parylene substrate, followed by PDMS encapsulation to maintain the intrinsic softness and flexibility required for contact-lens wear. A peripheral pHEMA-based commercial contact-lens material was subsequently molded to ensure wearing comfort and adequate oxygen permeability[56] (Fig. 2A).

Optical characterization showed that the visible-light transmittance of the central 5-mm region of Embobi exceeds 85% (Fig. 2B), remaining compatible with physiological pupil diameters under typical viewing conditions. For the earlier PDMS-substrate prototype, surface hydrophilicity was further improved by oxygen plasma treatment followed by immersion in a polyvinylpyrrolidone (PVP) solution, whereas the pHEMA-based substrate used in the final wearable design is intrinsically hydrophilic. Water contact-angle measurements revealed a substantial reduction from 105.5° to approximately 30° after surface modification, with the hydrophilic state remaining stable over one week (n = 5; Fig. 2C).

For improved wearing comfort and reduced risk of corneal irritation, the overall thickness of Embobi was controlled to below 100 μm, with smooth and compliant edges (Fig. 2D). Reliable monitoring of corneal curvature and gaze direction critically depends on the stability of the resonant signals; therefore, both mechanical fatigue and chemical stability were systematically evaluated. Cyclic loading tests demonstrated stable baseline resonant frequencies under 4,000 pressure cycles, corresponding to repetitive eyelid-induced forces such as blinking and occasional eye rubbing (Fig. 2E), as well as under 2,000 bending cycles that mimic mechanical stresses introduced during routine lens handling and pick-up (Fig. 2F). In addition, we examined the effect of frequent ocular rotations on the reflection coefficient. When the external readout coil was maintained in a stable position, no appreciable drift was observed in the linear S11 reflection coefficients of the three resonance peaks. To evaluate the repeatability of Embobi, 2000-cycle pitch and yaw rotation tests were performed (Supplementary Fig. 4). The mean standard deviations of the three Chs were 0.0018 and 0.0012 in the two tests, with maximum signal intensities of 0.8624 and 0.8690, respectively, demonstrating the excellent repeatability and stability of Embobi during repeated ocular movements. This mechanical robustness is attributed to the stable electrical conductivity of the copper coils and the low compressibility of the composite structure, while the chemical stability arises from the excellent water resistance of the PDMS and Parylene encapsulation layers.

The cytocompatibility of Embobi was further assessed using human corneal epithelial cells (HCE-T). Cells were cultured with Embobi extracts, negative control medium, and positive control medium, and cell viability was quantified after 24 h and 48 h of incubation, as detailed in the Methods section. As shown in Fig. 2H, cell viability in the Embobi extract group remained above 98% at both time points, with no significant difference compared to

the negative control (24 h, $p = 0.65$; 48 h, $p = 0.86$), whereas a pronounced reduction was observed relative to the positive control ($p < 0.0001$ at both 24 h and 48 h). Representative fluorescence microscopy images (Fig. 2I) further confirmed these results, showing abundant viable cells with intact morphology in both the Embobi and negative control groups at 24 h and 48 h, accompanied by increased cell density over time. In contrast, the positive control exhibited markedly reduced cell numbers and viability, validating the effectiveness of the cytotoxicity assay and demonstrating the favorable biocompatibility of Embobi.

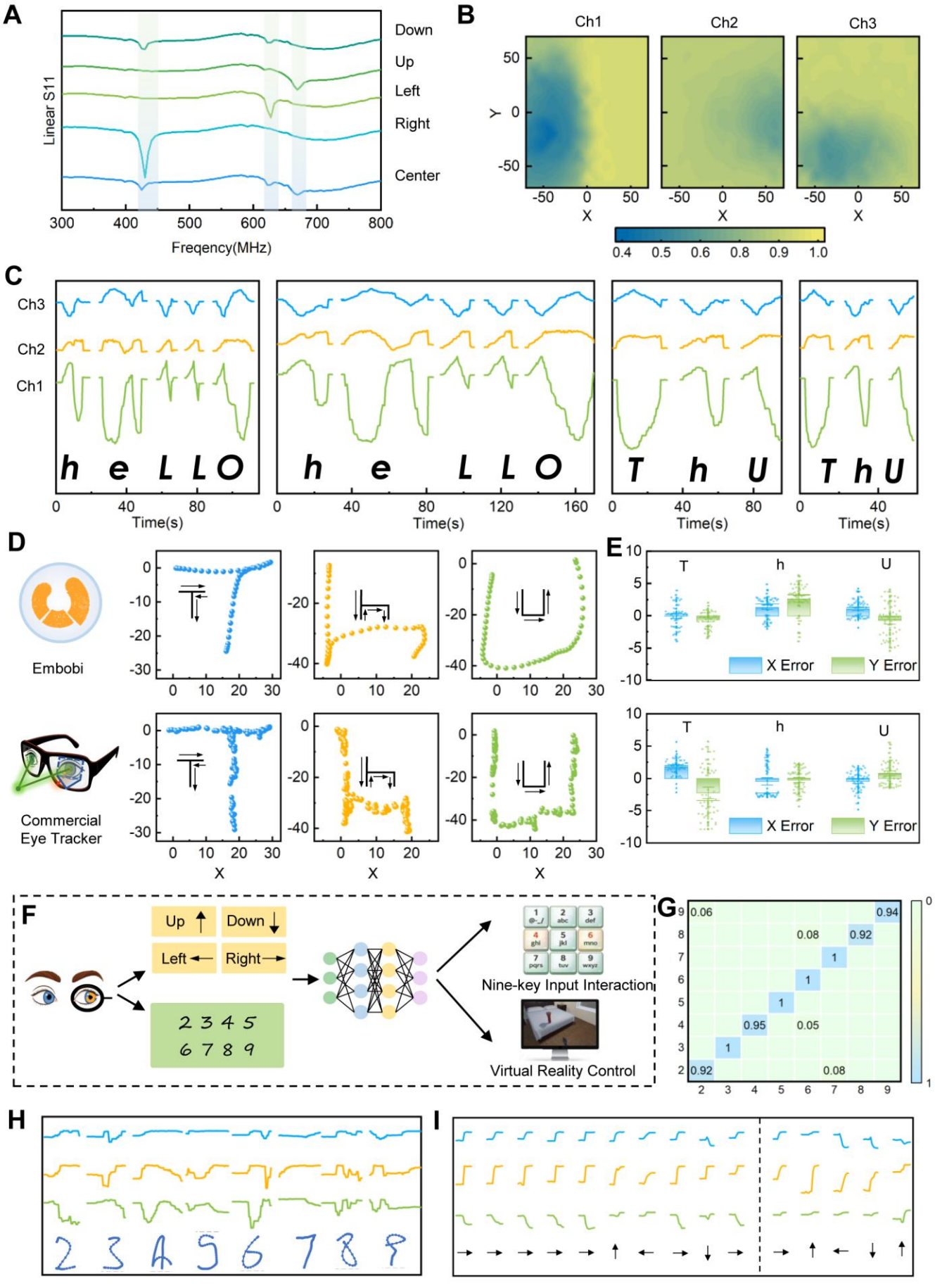

A
Linear S11
Down
Up
Left
Right
Center
300
400
500
600
700
800
Freqency(MHz)
B
Ch1
Ch2
Ch3
50
0
-50
Y
X
0.4
0.5
0.6
0.8
0.9
1.0
C
Ch3
Ch2
Ch1
h e L L O
h e L L O
T h U
T h U
Time(s)
D
Embobi
Commercial
Eye Tracker
X
E
T
h
U
X Error
Y Error
F
Up
Down
Left
Right
2 3 4 5
6 7 8 9
Nine-key Input Interaction
Virtual Reality Control
G
0.06
0.94
0.08
0.92
1
1
0.95
0.05
1
0.92
0.08
H
I

Fig. 3: Structural encoding, quantitative validation, and interaction deployment of gaze-direction signals in Embobi.
(A) Direction-dependent resonance spectra showing differential resonance-peak amplitudes across three channels (Ch1–Ch3) during controlled ocular rotations (up, down, left, right, and central). **(B)** Spatial distributions of resonance-peak amplitudes mapped onto the two-dimensional yaw–pitch gaze space from calibration data. **(C)** Multi-channel resonance-amplitude time series during gaze-based handwriting at different angular velocities, demonstrating velocity-invariant structural signatures. **(D)** Reconstructed angular gaze trajectories for writing "T", "h", and "U" using Embobi (top) and a commercial infrared eye tracker (bottom) under identical robotic-eye motion. **(E)** Error distributions of gaze-direction tracking along yaw and pitch axes for Embobi and the commercial tracker. **(F)** Schematic of direction-driven interaction pipelines enabled by continuous gaze-direction decoding, including nine-key ocular input and immersive VR control. **(G)** Confusion matrix of CNN-based classification accuracy for gaze-written digits in the nine-key paradigm. (H) Representative raw resonance-amplitude traces (Ch1–Ch3) during gaze-written digits (2–9). **(I)** Representative raw resonance-amplitude traces during gaze-direction commands for VR interaction.

Physically structured encoding of gaze direction at the ocular interface

Resolving three-dimensional gaze requires that directional orientation be stably encoded as a physical variable at the sensing interface. In Embobi, gaze direction is not inferred from optical imaging but directly structured through direction-dependent resonance-peak amplitude variations across three independent resonant channels (Ch1–Ch3). These variations arise from asymmetric near-field electromagnetic coupling within the chipless resonant array embedded in the smart contact lens, enabling illumination-independent and imaging-free direction sensing (Supplementary Fig. 5). We further evaluated the effects of reader-coil distance and blink-induced perturbation on the resonant spectra, with detailed analyses provided in Supplementary Figs. 6 and 7.

To quantitatively characterize directional encoding, a two-degree-of-freedom robotic eye platform was employed, allowing independent control of yaw and pitch without reliance on a display plane (Supplementary Fig. 8, X coordinate, yaw angle; Y coordinate, pitch angle). During calibration, the robotic eye traversed a spiral trajectory spanning the physiological oculomotor range, with increased sampling density near the central orientation to enhance angular resolution for natural viewing behavior.

As shown in Fig. 3A, upward, downward, leftward, and rightward rotations generate distinct differential amplitude responses across the three resonance channels. These structured spectral signatures constitute the physical basis for direction decoding. The corresponding amplitude distributions mapped onto the two-dimensional yaw–pitch space (Fig. 3B) exhibit complementary and spatially distinguishable sensitivity profiles among Ch1–Ch3, enabling robust discrimination of gaze orientations.

Using calibration data pairs of resonance amplitudes and ground-truth gaze angles, supervised regression models were trained to independently reconstruct yaw and pitch trajectories (Supplementary Fig.9). The decoded trajectories demonstrate stable performance under dynamic conditions. During continuous gaze-based handwriting at different angular velocities, the multi-channel resonance signals preserve letter-specific structural patterns while scaling proportionally in time (Fig. 3C), indicating that Embobi captures continuous gaze dynamics rather than discrete event transitions.

Quantitative validation against commercial eye tracking

To benchmark directional tracking performance, identical angular trajectories corresponding to the letters "T", "h", and "U" were executed by the robotic eye and reconstructed using both Embobi and a commercial infrared reflection–based eye tracker. We further evaluated the influence of contact-lens rotational orientation on directional decoding accuracy, with detailed results provided in Supplementary Fig.10. As shown in Fig. 3D, both systems recover the global stroke morphology; however, trajectories reconstructed by Embobi exhibit smoother continuity with reduced high-frequency jitter, particularly during small-amplitude movements near the central orientation.

Error statistics relative to ground-truth angular references (Fig. 3E) show that the standard deviation of angular errors along both yaw and pitch axes remains within 1°, placing Embobi in the same accuracy range as commercial

optical systems. Notably, this performance is achieved without cameras, infrared illumination, or environmental calibration, underscoring that gaze direction is physically structured and decoded at the sensing node rather than reconstructed through imaging pipelines.

Direction signals as continuous perceptual interaction variables

Because gaze direction is resolved as a continuous physical signal, it can directly organize interaction without discrete dwell-based triggering. In a nine-key ocular-input paradigm (Fig. 3F, Supplementary Fig.11), digits are encoded through continuous gaze-written trajectories and classified using a lightweight convolutional neural network, achieving a validation accuracy of 96.4% (Fig. 3G). Representative raw resonance-amplitude traces for gaze-written digits 2–9 (Fig. 3H) exhibit consistent, class-distinguishable temporal structures across the three channels.

We further evaluated continuous direction decoding in an immersive virtual-reality control task under completely dark conditions (Fig. 3F), demonstrating a key advanChe of the Embobi system over conventional eye trackers that rely on illumination. Using only four directional gaze signals (up, down, left, and right), the system supported 10 rounds of robotic viewpoint control and 5 rounds of turning-and-walking navigation, achieving a 100% control success rate across all trials. Representative multi-channel traces during directional commands (Fig. 3I) confirmed stable signal acquisition throughout interactive operation. These results demonstrate that our system maintains robust gaze-driven interaction even in light-deprived environments. Together, these demonstrations show that direction, when physiologically encoded and directly decoded at the ocular interface, can serve as a continuous perceptual state that dynamically structures system behavior.

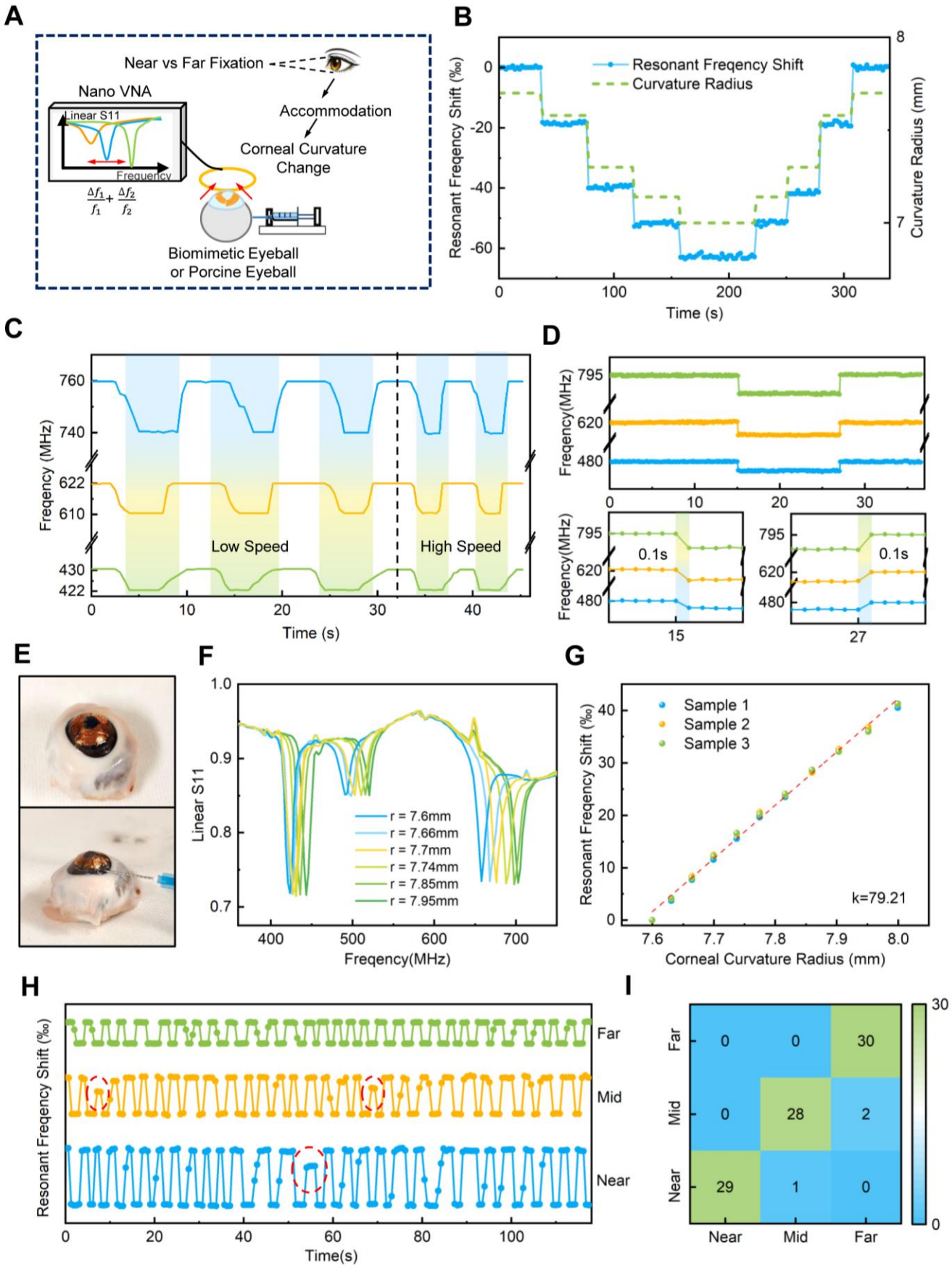


Fig. 4: Resonance-based sensing of accommodation-related corneal curvature variation in Embobi.

(A) Schematic of the experimental framework. Near-versus-far fixation induces accommodation, leading to corneal curvature change that is transduced by the smart contact lens into resonance-frequency shifts and wirelessly interrogated using a NanoVNA. **(B)** Real-time averaged resonance-frequency shift (coils 1 and 2) and corresponding curvature radius during stepwise modulation. **(C)** Frequency responses under low-speed and high-speed curvature transitions. **(D)** Multi-channel resonance spectra during curvature change; bottom panels show magnified transition regions. **(E)** Ex vivo porcine eye experiments demonstrating biological validation. **(F)** Representative Linear |S11| spectra measured at different corneal curvature radii, showing systematic resonance shifts. **(G)** Reproducibility of curvature sensitivity across three independent devices tested on biological tissue. **(H)** Repeated water-lens modulation experiments across three discrete curvature states corresponding to Near, Mid and Far focal planes, showing stable and separable resonance-frequency shifts over 3 × 30 trials. **(I)** Confusion matrix for focal-plane classification based on the averaged resonance-frequency shift.

Physiological decoding of fixation depth through curvature-dependent resonance shifts

Accommodation involves coordinated biomechanical responses of the anterior ocular segment, including subtle but systematic changes in corneal curvature. In Embobi, fixation-depth information is derived from sensing these curvature-related deformations through resonance-frequency shifts of embedded planar spiral coils. Wireless interrogation is performed using a NanoVNA, which reports the reflected signal as the linear magnitude of the reflection coefficient (Linear |S11|); resonance frequencies are extracted from the minima of the |S11| spectrum. Because coils 1 and 2 share identical geometries but differ in scale, they respond in common mode to global curvature variation. Accordingly, fixation-depth characterization in this section is quantified using the averaged resonance-frequency shift of coils 1 and 2, excluding coil 3 (see Supplementary Note S1 for rationale).

We first established curvature–frequency coupling using a controllable water-lens eye model (Fig. 4A). Stepwise modulation of the corneal curvature radius produces monotonic shifts in resonant frequency (Fig. 4B), with stable and reversible tracking during dynamic transitions at both low and high modulation speeds (Fig. 4C). Multi-channel spectra (Fig. 4D) further confirm synchronous frequency variation of coils 1 and 2 under curvature deformation, consistent with their common-mode design. Owing to the high sensitivity of the RLC resonant system to curvature-induced changes in inductance and capacitance, even small physiological curvature variations generate measurable spectral shifts. For example, a curvature-radius change of approximately 50 μm—within the range reported during human accommodation—corresponds to resonance-frequency shifts of approximately 2.18–3.14 MHz across the two sensing coils. These shifts are substantially larger than resonance drift induced by temperature variation or environmental perturbations (Supplementary Fig. 12, 13), enabling reliable detection of curvature modulation.

Representative Linear |S11| spectra measured at different curvature radii are shown in Fig. 4F. Within the small curvature variations relevant to physiological accommodation, the resonance minima shift systematically while the resonance magnitude remains nearly unchanged. This indicates that curvature information is primarily encoded in the resonance position rather than resonance magnitude, allowing curvature sensing to remain largely decoupled from the direction-sensing channel. This decoupling is further supported by multi-channel spectral maps acquired during eye rotation under different curvature states, which show that resonance frequencies remain stable during rotation while the directional channel responses are preserved (Supplementary Fig. 14). Additional electromagnetic simulations (HFSS) further support the robustness of resonance-frequency shifts as an indicator of curvature variation (Supplementary Fig.15).

To evaluate performance in biologically realistic tissue, we conducted measurements on ex vivo porcine eyeballs (Fig. 4E). Controlled deformation of the porcine cornea produced resonance-frequency shifts following the same monotonic trend observed in the synthetic model (Fig. 4F). Prior ophthalmic studies summarized in Supplementary Note S1 indicate that accommodation from far to near fixation typically induces corneal curvature-radius changes on the order of 50–100 μm[40,45]. The curvature ranges investigated in Fig. 4F–G (approximately 7.6–8.0 mm radius) therefore correspond closely to the physiological human regime. Within this range, the device

exhibits a strong linear response with minimal hysteresis and stable slope characteristics. Repeated measurements across three independently fabricated devices show consistent curvature sensitivity (Fig. 4G), indicating reproducible performance on biological substrates. To further evaluate whether these curvature-dependent resonance shifts can support robust depth-state decoding, we performed repeated water-lens modulation experiments across three discrete curvature states corresponding to Near, Mid and Far focal planes (Fig. 4H). Across 3×30 trials, the averaged resonance-frequency shift remained well separated among the three states, with only occasional boundary-level overlap. Classification based on the resonance shift yielded an overall focal-plane decoding accuracy above 96% (Fig. 4I), confirming reliable discrimination of physiologically relevant depth states.

Because accommodation typically occurs as transitions between physiologically distinguishable focusing states, curvature sensing naturally resolves discrete accommodative focal planes, consistent with the high decoding accuracy across the Near/Mid/Far states (Fig. 4H,I). To support this interaction-oriented interpretation, calibration of a water-lens phantom establishes a monotonic mapping between curvature radius and discrete equivalent focal planes (Near/Mid/Far), as summarized in Supplementary Fig.16. Such physiologically grounded depth states are well suited to interactive scenarios—such as variable-focus virtual and augmented reality—where depth-aware interaction does not require continuous millimeter-scale distance estimation. In this framework, Embobi measures the underlying biomechanical signal associated with accommodation itself, providing a mechanically grounded and externally accessible representation of fixation depth.

Together, these results demonstrate that accommodation-scale corneal curvature variations can be robustly transduced into resonance-frequency shifts using the Embobi contact lens platform. This provides a direct physiological encoding pathway for fixation depth, bypassing geometric triangulation or scene reconstruction used in conventional gaze-tracking systems. By combining direction sensing (Fig. 3) with curvature-derived depth information at the sensing interface, Embobi enables reconstruction of three-dimensional points of regard in space.

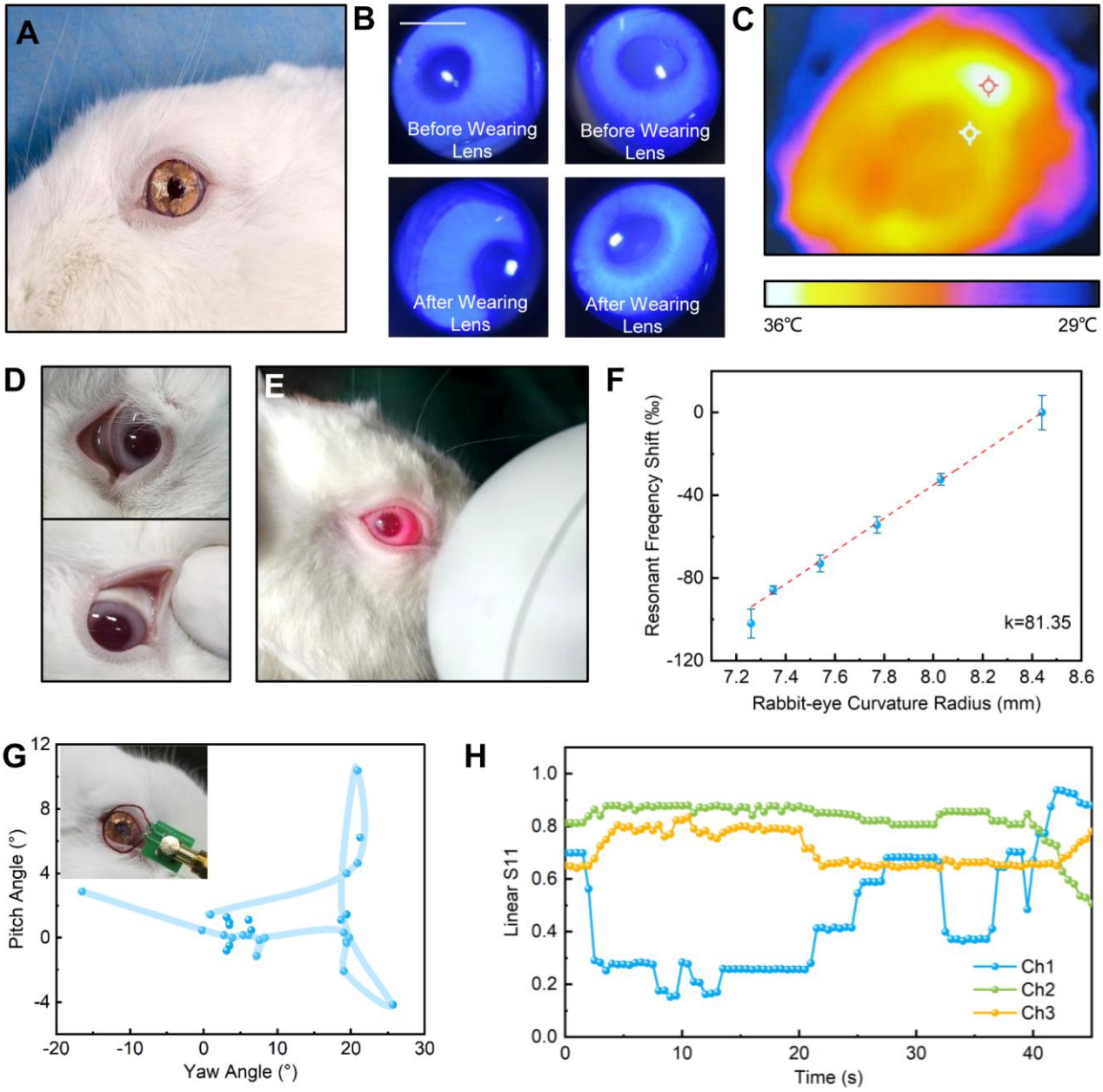


Fig. 5: In vivo rabbit validation of Embobi: ocular compatibility and functional verification of curvature and direction channels.

(A) Photograph of a rabbit wearing Embobi. **(B)** Slit-lamp images of rabbit corneas before and after continuous wear. **(C)** Infrared thermography of the ocular surface during operation, showing temperature within physiological range. **(D)** Photographs of the upper and lower eyelids after 48 h of continuous wear. **(E)** Clinical infrared keratometer used for in vivo measurement of rabbit corneal curvature. **(F)** Resonance-frequency dependence on rabbit-eye corneal curvature radius measured in vivo. **(G)** Representative reconstructed gaze-direction trajectory (yaw and pitch) from rabbit-eye rotation tests (inset: experimental setup). **(H)** Multi-channel resonance amplitude signals (Ch1–Ch3) recorded during in vivo eye movements.

To evaluate the in vivo feasibility and ocular compatibility of Embobi, we performed rabbit-eye experiments involving extended wear and physiological signal readout. Representative photographs of rabbits wearing the device are shown in Fig. 5A. Slit-lamp examination before and after continuous wear revealed no observable corneal edema, opacity, or epithelial damage (Fig. 5B; Supplementary Fig.17). Infrared thermography further

confirmed that the ocular surface temperature remained within the physiological range during operation (Fig. 5C), consistent with the passive and chipless architecture of the device, which eliminates active heat generation. After 48 hours of wear, inspection of the upper and lower eyelids showed no visible inflammation or structural damage (Fig. 5D, Supplementary Fig.18), indicating good short-term ocular compatibility.

Because controlled three-dimensional fixation tasks are difficult to induce reliably in rabbits, the curvature-sensing and direction-sensing channels were validated independently in vivo. We first examined corneal curvature sensing on living eyes. Rabbit corneal curvature was independently measured using a clinical infrared keratometer as a reference measurement (Fig. 5E), while the corresponding resonance frequencies of the Embobi device were recorded in situ. Posture-dependent changes in rabbit corneal curvature were used to evaluate the relationship between resonance frequency and physiological curvature, and to validate the sensitivity of Embobi for corneal-curvature monitoring under normal physiological conditions (Supplementary Fig. 19). Corneal curvature was quantified in the supine position and at 30° and 45° inclinations to generate physiologically relevant variations. To extend the curvature window, anterior chamber perfusion with saline was further performed to reduce corneal curvature. As shown in Fig. 5F, the resonance-frequency shift exhibits a clear monotonic dependence on rabbit-eye corneal curvature radius, consistent with the trends observed in the synthetic eye model and ex vivo porcine experiments (Fig. 4). Within the physiological curvature range of the rabbit cornea, the device maintains a stable and approximately linear response, confirming that curvature-related biomechanical deformation can be reliably detected in vivo.

In parallel, the direction-sensing capability of Embobi was evaluated through eye-rotation experiments in rabbits. Representative reconstructed yaw–pitch trajectories demonstrate that ocular rotations can be continuously resolved under physiological conditions (Fig. 5G). Corresponding multi-channel resonance amplitude signals recorded during eye movements show stable and channel-specific modulation patterns (Fig. 5H), indicating that the direction-sensitive channels remain well separated during in vivo operation.

Together, these results demonstrate that Embobi can be safely worn while maintaining stable in vivo readout of both curvature-related and direction-related physiological signals. The validated sensing channels provide the basis for integrating depth-related and directional information at the sensing interface, enabling subsequent reconstruction of three-dimensional points of regard.

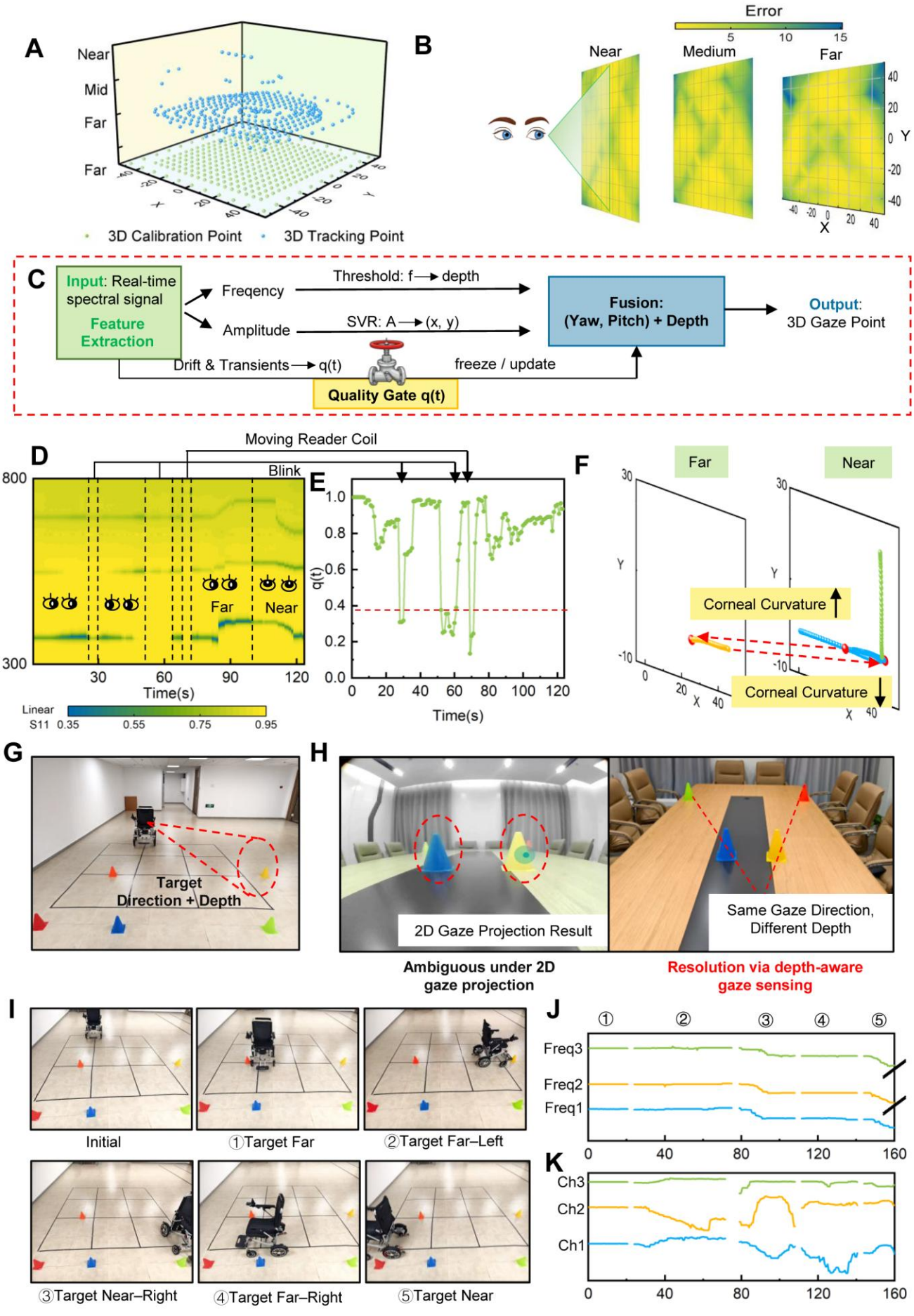

A
Near
Mid
Far
Far
3D Calibration Point
3D Tracking Point
B
Error
5
10
15
Near
Medium
Far
C
Input: Real-time spectral signal
Feature Extraction
Freqency
Amplitude
Threshold: f → depth
SVR: A → (x, y)
Fusion: (Yaw, Pitch) + Depth
Output: 3D Gaze Point
Drift & Transients → q(t)
freeze / update
Quality Gate q(t)
D
Moving Reader Coil
Blink
Far
Near
Time(s)
Linear
S11 0.35 0.55 0.75 0.95
E
q(t)
Time(s)
F
Far
Near
Corneal Curvature
Corneal Curvature
G
Target Direction + Depth
H
2D Gaze Projection Result
Same Gaze Direction, Different Depth
Ambiguous under 2D gaze projection
Resolution via depth-aware gaze sensing
I
Initial
①Target Far
②Target Far–Left
③Target Near–Right
④Target Far–Right
⑤Target Near
J
Freq3
Freq2
Freq1
K
Ch3
Ch2
Ch1

Fig. 6: Joint reconstruction of three-dimensional points of regard and perception-driven spatial interaction **(A)** Spatial distribution of reconstructed 3D gaze points relative to calibrated ground-truth targets. **(B)** Heatmaps of 3D localization error under near, intermediate, and far fixation conditions, showing bounded error across depth planes. **(C)** Edge-level fusion architecture integrating amplitude-derived direction features and frequency-derived depth features with quality gating q(t). **(D)** Representative raw spectral evolution under dynamic conditions, including blink and reader-coil disturbance. **(E)** Time-varying quality factor q(t) demonstrating freeze–update gating during transient artifacts. **(F)** Depth-resolved gaze points reconstructed by the edge-level fusion algorithm, illustrating 3D point-of-regard localization across two representative fixation depths. **(G)** Real-world wheelchair navigation scenario driven by 3D gaze targets. **(H)** Comparison between conventional 2D gaze projection (left) and depth-aware gaze sensing (right) in occluded or cluttered environments. **(I)** Sequential snapshots of 3D target-driven wheelchair navigation. **(J–K)** Representative multi-channel frequency and amplitude traces during spatial interaction tasks.

Three-dimensional point-of-regard reconstruction and spatial localization

Having independently validated direction encoding (Fig. 3), curvature-derived depth encoding (Fig. 4), and in vivo physiological readout (Fig. 5), we next integrate these signals to reconstruct three-dimensional points of regard (3D PoR) in space.

Figure 6A shows the spatial distribution of predicted 3D gaze points relative to calibrated ground-truth targets. Across the interaction volume, reconstructed points cluster tightly around their corresponding calibration positions, demonstrating stable spatial localization from fused direction and depth signals.

To evaluate depth robustness, we quantified 3D localization error under near, intermediate, and far fixation conditions (Fig. 6B). Error heatmaps reveal that reconstruction accuracy remains spatially bounded across all depth planes, without the dramatic error amplification typically associated with direction-only formulations (Supplementary Fig. 20). Unlike conventional binocular triangulation, in which angular uncertainty leads to increasing positional error at longer fixation distances, Embobi maintains comparable error distributions across depth conditions by incorporating a physiologically encoded depth coordinate.

The real-time fusion architecture is illustrated in Fig. 6C. Spectral signals are decomposed into frequency-derived depth features and amplitude-derived direction features. A lightweight regression module estimates yaw–pitch angles from multi-channel amplitudes, while frequency shifts are mapped to curvature-derived depth. To ensure robustness against blink artifacts, transient interference, or reader-coil displacement, a time-varying quality factor q(t) is computed and used to gate updates. When q(t) falls below threshold, the system temporarily freezes spatial updates, preventing spurious 3D point outputs. Representative signal evolution from raw spectral data to final 3D output is shown in Fig. 6D–F, illustrating suppression of transient disturbances and stable recovery.

Depth-aware spatial interaction beyond conventional 2D eye tracking

With three-dimensional gaze localization established, we demonstrate perception-driven spatial interaction in real-world scenarios. In a target-driven wheelchair navigation task (Fig. 6G, I, Supplementary Fig.21, 22), user intent is specified by fixating a spatial target rather than issuing sequential directional commands. Once a 3D fixation point is resolved, navigation is initiated toward that target location. Direction determines heading, while depth modulates traveling distance, enabling intuitive “look-to-go” control without explicit left–right–forward command translation. This is achieved through a water lens and rotational platform system that simulates the joint changes in corneal curvature and gaze direction.

To further evaluate target discrimination in a cluttered spatial scene, we arranged cone-shaped targets at different depths along nearly the same line of sight (Fig. 6H). In this setting, the commercial eye tracker Sol glasses produced an ambiguous 2D gaze projection because the candidate targets were separated mainly in depth and only minimally in angle. Embobi, by contrast, incorporated fixation-depth estimation together with gaze direction and therefore resolved the correct target in the same scene.

Together, these results demonstrate that by structuring fixation as a three-dimensional perceptual coordinate, Embobi enables stable spatial localization and interaction dynamics directly grounded in physiological encoding.

Comparison Metric	Embobi	Meta Aria Gen 2
Form Factor	Invisible	Visible
Weight	< 1 g	~75 g
Power Consumption	**Negligible** on-lens power consumption	Estimated hundreds of mW, 6-8h battery life
Hardware Resources	3 copper coil arrays	4 CV cameras, 2 eye-tracking cameras, 8 microphones, IMUs, GNSS, PPG, ALS
Eye Tracking	Stable gaze accuracy; **performs better in scenarios with minimal gaze angle and large depth differences**	2-eye triangulation for gaze direction; **affected by gaze angle and occlusion**
3D Gaze Sensing	**Direct depth estimation** from corneal deformation	Estimated depth via **binocular triangulation** and scene geometry
Interaction Modes	Gaze-based writing, VR interaction, wheelchair navigation	Voice commands , environment perception

Table 2. Comparison of Embobi with representative head-worn sensing platforms

Unlike conventional head-worn devices focused on visual display or spatial computing, such as XREAL Air, Microsoft HoloLens, or Apple Vision Pro, Embobi is developed as an eye-centric sensing platform. As summarized in Table 2, its representative advantages include an invisible form factor, sub-gram weight, negligible on-lens power consumption, and direct 3D gaze sensing enabled by corneal deformation. Embobi therefore represents a distinct class of bio-integrated ocular interface, rather than a display- or computation-driven wearable.

Discussion

In this work, Embobi demonstrates that three-dimensional gaze can be resolved at the ocular interface as a physiologically grounded perceptual state, rather than reconstructed as a computational variable. Beyond achieving robust 3D gaze reconstruction, the significance of this work lies in reconfiguring where and how perceptual variables are structured within an eye–machine system. By embedding accommodation directly into the sensing architecture, fixation depth becomes a measurable coordinate intrinsic to the interface itself, shifting gaze tracking from downstream correction toward source-level stabilization.

From this perspective, the significance of this work lies in enabling robust three-dimensional gaze localization with low power consumption and a simplified hardware architecture, without requiring chips, scene cameras, or binocular sensing. Rather than relying on increasingly elaborate computation, Embobi captures gaze direction and fixation depth as separable physical signals at the sensing node. This design improves robustness by limiting the rapid growth of depth error with viewing distance and reducing sensitivity to ambient lighting conditions. The co-design of lens mechanics, resonant structures, gaze decoding algorithms, and lightweight signal processing further supports practical operation in wearable, spatially distributed interaction scenarios.

More importantly, resolving gaze as a physiologically grounded three-dimensional point of regard alters the logic of interaction itself. Conventional gaze interfaces treat gaze as a two-dimensional projection that must be translated into discrete symbolic commands[57,58]. In contrast, Embobi uses the user's three-dimensional fixation state as a direct basis for control. Interaction no longer depends primarily on dwell-time thresholds or explicit selection heuristics, but can be guided by stable fixation in depth-rich space. In this sense, perceptual states more directly shape how the system responds to the user.

This perception-driven interaction fundamentally changes how ambiguity is managed in real-world environments. When multiple objects share similar viewing directions but differ in depth, two-dimensional gaze projection cannot uniquely specify intent. By incorporating fixation depth at the perceptual level, Embobi enables target specification through spatial fixation rather than command translation. Across text entry, immersive navigation, and assistive mobility scenarios, system control shifts from event-triggered actions to continuous perceptual coupling. Practical deployment may incorporate fixation stability thresholds or context-aware gating to distinguish intentional engagement from incidental gaze, ensuring safe and reliable operation.

The embodied sensing strategy also introduces translational considerations. In vivo experiments in freely moving rabbits confirm that accommodation-related corneal signals can be captured under natural physiological conditions, and biocompatibility assessments indicate stable wear over the tested period. Nevertheless, long-term human validation, inter-subject variability in corneal biomechanics, and environmental electromagnetic interference represent important areas for further study. Refinements in coil geometry, material optimization, and adaptive decoding algorithms may further enhance signal stability and comfort.

More broadly, Embobi suggests a sensing framework in which intrinsic physiological processes are directly harnessed at the hardware interface, bringing perception and interaction into closer alignment. By treating three-dimensional fixation states as direct control signals, this work outlines a pathway toward spatially grounded eye–machine systems in which interaction is guided more directly by perception than by symbolic command selection. More broadly, this work points toward human-centered interfaces that enable more natural and seamless interaction by sensing and leveraging the user's physiological, cognitive, and behavioral states.

References

1. Jacob, R. J. K. & Karn, K. S. Eye Tracking in Human-Computer Interaction and Usability Research. in *The Mind's Eye* 573–605 (Elsevier, 2003). doi:10.1016/B978-044451020-4/50031-1.
2. Majaranta, P. & Räihä, K.-J. Twenty years of eye typing: systems and design issues. in *Proceedings of the symposium on Eye tracking research & applications - ETRA '02* 15 (ACM Press, New Orleans, Louisiana, 2002). doi:10.1145/507072.507076.
3. Zhu, H. *et al.* Frequency-encoded eye tracking smart contact lens for human–machine interaction. *Nat Commun* **15**, 3588 (2024).
4. Slater, M. & Sanchez-Vives, M. V. Enhancing Our Lives with Immersive Virtual Reality. *Front. Robot. AI* **3**, (2016).
5. Billinghurst, M., Clark, A. & Lee, G. A Survey of Augmented Reality. *Foundations and Trends® in Human—Computer Interaction* **8**, 73–272 (2015).
6. Weiser, M. The Computer for the 21st Century. *Sci Am* **265**, 94–104 (1991).
7. Pfeifer, R., Lungarella, M. & Iida, F. Self-Organization, Embodiment, and Biologically Inspired Robotics. *Science* **318**, 1088–1093 (2007).
8. Cheng, Y., Wang, H., Bao, Y. & Lu, F. Appearance-Based Gaze Estimation With Deep Learning: A Review and Benchmark. *IEEE Trans. Pattern Anal. Mach. Intell.* **46**, 7509–7528 (2024).
9. Liu, J., Chi, J., Yang, H. & Yin, X. In the eye of the beholder: A survey of gaze tracking techniques. *Pattern Recognition* **132**, 108944 (2022).
10. Davalos, E. *et al.* 3D Gaze Tracking for Studying Collaborative Interactions in Mixed-Reality Environments. in *Companion Proceedings of the 26th International Conference on Multimodal Interaction* 175–183 (ACM, San Jose Costa Rica, 2024). doi:10.1145/3686215.3688380.
11. Sun, Z., Zhu, M., Shan, X. & Lee, C. Augmented tactile-perception and haptic-feedback rings as human-machine interfaces aiming for immersive interactions. *Nat Commun* **13**, 5224 (2022).
12. Hansen, D. W. & Qiang Ji. In the Eye of the Beholder: A Survey of Models for Eyes and Gaze. *IEEE Trans. Pattern Anal. Mach. Intell.* **32**, 478–500 (2010).
13. Cui, K. *et al.* Advancements in Eye-Tracking for Machine Direction Control: Applications, Approaches, and Challenges. *Proceedings of the Human Factors and Ergonomics Society Annual Meeting* **69**, 762–767 (2025).
14. Hennessey, C. & Lawrence, P. Noncontact Binocular Eye-Gaze Tracking for Point-of-Gaze Estimation in Three Dimensions. *IEEE Trans. Biomed. Eng.* **56**, 790–799 (2009).
15. Gromilin, G. I., Kosykh, V. P. & Yakovenko, N. S. New algorithm for determining 3D coordinates of the eye cornea center in a non -contact eye-tracking system. in *2022 VIII International Conference on Information Technology and Nanotechnology (ITNT)* 1–4 (IEEE, Samara, Russian Federation, 2022). doi:10.1109/ITNT55410.2022.9848733.
16. Guestrin, E. D. & Eizenman, M. General Theory of Remote Gaze Estimation Using the Pupil Center and Corneal Reflections. *IEEE Trans. Biomed. Eng.* **53**, 1124–1133 (2006).
17. Elmadjian, C., Shukla, P., Tula, A. D. & Morimoto, C. H. 3D gaze estimation in the scene volume with a head-mounted eye tracker. in *Proceedings of the Workshop on Communication by Gaze Interaction* 1–9 (ACM, Warsaw Poland, 2018). doi:10.1145/3206343.3206351.
18. Sugano, Y., Matsushita, Y. & Sato, Y. Learning-by-Synthesis for Appearance-Based 3D Gaze Estimation. in *2014 IEEE Conference on Computer Vision and Pattern Recognition* 1821–1828 (IEEE, Columbus, OH, USA, 2014). doi:10.1109/CVPR.2014.235.
19. Chong, E. *et al.* Detecting Gaze Towards Eyes in Natural Social Interactions and Its Use in Child Assessment. *Proc. ACM Interact. Mob. Wearable Ubiquitous Technol.* **1**, 1–20 (2017).
20. Chong, E., Wang, Y., Ruiz, N. & Rehg, J. M. Detecting Attended Visual Targets in Video. in *2020 IEEE/CVF Conference on Computer Vision and Pattern Recognition (CVPR)* 5395–5405 (IEEE, Seattle, WA, USA, 2020). doi:10.1109/CVPR42600.2020.00544.
21. McAnally, K., Grove, P. & Wallis, G. Vergence eye movements in virtual reality. *Displays* **83**, 102683 (2024).
22. Pijpaert, A. R. *et al.* A validation study on the accuracy and precision of gaze and vergence using stereoscopic eye-tracking technology. *Behav Res* **57**, 214 (2025).
23. Wang, X., Holmqvist, K. & Alexa, M. The mean point of vergence is biased under projection. *JEMR* **12**, (2019).
24. Plopski, A. *et al.* The Eye in Extended Reality: A Survey on Gaze Interaction and Eye Tracking in Head-worn Extended Reality. *ACM Comput. Surv.* **55**, 1–39 (2023).
25. Cazzato, D., Leo, M., Distante, C. & Voos, H. When I Look into Your Eyes: A Survey on Computer Vision Contributions for Human Gaze Estimation and Tracking. *Sensors* **20**, 3739 (2020).
26. Bao, Y. & Lu, F. From Feature to Gaze: A Generalizable Replacement of Linear Layer for Gaze Estimation. in *2024 IEEE/CVF Conference on Computer Vision and Pattern Recognition (CVPR)* 1409–1418 (IEEE, Seattle, WA, USA, 2024). doi:10.1109/CVPR52733.2024.00140.

27. Chong, E. *et al.* Connecting Gaze, Scene, and Attention: Generalized Attention Estimation via Joint Modeling of Gaze and Scene Saliency. in *Computer Vision – ECCV 2018* (eds Ferrari, V., Hebert, M., Sminchisescu, C. & Weiss, Y.) vol. 11209 397–412 (Springer International Publishing, Cham, 2018).
28. Tonini, F., Dall'Asen, N., Beyan, C. & Ricci, E. Object-aware Gaze Target Detection. in *2023 IEEE/CVF International Conference on Computer Vision (ICCV)* 21803–21812 (IEEE, Paris, France, 2023). doi:10.1109/ICCV51070.2023.01998.
29. Lento, B. *et al.* 3D-ARM-Gaze: a public dataset of 3D Arm Reaching Movements with Gaze information in virtual reality. *Sci Data* **11**, 951 (2024).
30. Arefin, M. S., Swan, J. E., Hoffing, R. C. & Thurman, S. Mapping Eye Vergence Angle to the Depth of Real and Virtual Objects as an Objective Measure of Depth Perception. Preprint at https://doi.org/10.48550/ARXIV.2311.09242 (2023).
31. Lu, C., Chakravarthula, P., Tao, Y., Chen, S. & Fuchs, H. Improved vergence and accommodation via Purkinje Image tracking with multiple cameras for AR glasses. in *2020 IEEE International Symposium on Mixed and Augmented Reality (ISMAR)* 320–331 (IEEE, Porto de Galinhas, Brazil, 2020). doi:10.1109/ISMAR50242.2020.00058.
32. Hayhoe, M. & Ballard, D. Eye movements in natural behavior. *Trends in Cognitive Sciences* **9**, 188–194 (2005).
33. Schor, C. M., Alexander, J., Cormack, L. & Stevenson, S. Negative feedback control model of proximal convergence and accommodation. *Ophthalmic and Physiological Optics* **12**, 307–318 (1992).
34. Fincham, E. F. & Walton, J. The reciprocal actions of accommodation and convergence. *The Journal of Physiology* **137**, 488–508 (1957).
35. Campbell, F. W. & Westheimer, G. Dynamics of accommodation responses of the human eye. *The Journal of Physiology* **151**, 285–295 (1960).
36. Croft, M. A., Glasser, A. & Kaufman, P. L. Accommodation and Presbyopia.
37. Schachar, R. A. & Bax, A. J. Mechanism of Accommodation: *International Ophthalmology Clinics* **41**, 17–32 (2001).
38. Koretz, J. F., Kaufman, P. L., Neider, M. W. & Goeckner, P. A. Accommodation and presbyopia in the human eye—aging of the anterior segment. *Vision Research* **29**, 1685–1692 (1989).
39. Koke, M. P. MECHANISM OF ACCOMMODATION. *Archives of Ophthalmology* **27**, 950–968 (1942).
40. He, J. C., Gwiazda, J., Thorn, F., Held, R. & Huang, W. Change in corneal shape and corneal wave-front aberrations with accommodation. *Journal of Vision* **3**, 1 (2003).
41. Wallace, H. B., McKelvie, J., Green, C. R. & Misra, S. L. Corneal Curvature: the Influence of Corneal Accommodation and Biomechanics on Corneal Shape. *Trans. Vis. Sci. Tech.* **8**, 5 (2019).
42. Popiolek-Masajada, A., Pierscionek, B. K. & Kasprzak, H. T. Cornea shape and accommodation. in (eds Perina, Sr., J., Hrabovsky, M. & Krepelka, J.) 364–366 (Velke Losiny, Czech Republic, 2001). doi:10.1117/12.417855.
43. Pierścionek, B. K., Popiolek-Masajada, A. & Kasprzak, H. Corneal shape change during accommodation. *Eye* **15**, 766–769 (2001).
44. Sisó-Fuertes, I., Domínguez-Vicent, A., Del Águila-Carrasco, A., Ferrer-Blasco, T. & Montés-Micó, R. Corneal changes with accommodation using dual Scheimpflug photography. *Journal of Cataract and Refractive Surgery* **41**, 981–989 (2015).
45. Yasuda, A., Yamaguchi, T. & Ohkoshi, K. Changes in corneal curvature in accommodation. *Journal of Cataract and Refractive Surgery* **29**, 1297–1301 (2003).
46. Hung, G. K. Adaptation model of accommodation and vergence. *Ophthalmic Physiologic Optic* **12**, 319–326 (1992).
47. Park, J. *et al.* Soft, smart contact lenses with integrations of wireless circuits, glucose sensors, and displays. *Sci. Adv.* **4**, eaap9841 (2018).
48. Leonardi, M., Leuenberger, P., Bertrand, D., Bertsch, A. & Renaud, P. First Steps toward Noninvasive Intraocular Pressure Monitoring with a Sensing Contact Lens. *Invest. Ophthalmol. Vis. Sci.* **45**, 3113 (2004).
49. Muntz, A., Subbaraman, L. N., Sorbara, L. & Jones, L. Tear exchange and contact lenses: A review. *Journal of Optometry* **8**, 2–11 (2015).
50. Abass, A. *et al.* Simulated optical performance of soft contact lenses on the eye. *PLoS ONE* **14**, e0216484 (2019).
51. Massin, L. *et al.* Smart Contact Lens Applied to Gaze Tracking. *IEEE Sensors J.* **21**, 455–463 (2021).
52. Khaldi, A. *et al.* A laser emitting contact lens for eye tracking. *Sci Rep* **10**, 14804 (2020).
53. Li, L. *et al.* SmartLens: sensing eye activities using zero-power contact lens. in *Proceedings of the 28th Annual International Conference on Mobile Computing And Networking* 473–486 (ACM, Sydney NSW Australia, 2022). doi:10.1145/3495243.3560532.
54. Gan, X. *et al.* Closed-eye intraocular pressure and eye movement monitoring via a stretchable bimodal contact lens. *Microsyst Nanoeng* **11**, 83 (2025).
55. Massin, L., Lahuec, C., Seguin, F., Nourrit, V. & De Bougrenet De La Tocnaye, J.-L. Multipurpose Bio-Monitored Integrated Circuit in a Contact Lens Eye-Tracker. *Sensors* **22**, 595 (2022).
56. Wichterle, O. & Lím, D. Hydrophilic Gels for Biological Use. *Nature* **185**, 117–118 (1960).

57. Majaranta, P. & Bulling, A. Eye Tracking and Eye-Based Human–Computer Interaction. in *Advances in Physiological Computing* (eds Fairclough, S. H. & Gilleade, K.) 39–65 (Springer London, London, 2014). doi:10.1007/978-1-4471-6392-3_3.
58. Lei, Y., He, S., Khamis, M. & Ye, J. An End-to-End Review of Gaze Estimation and its Interactive Applications on Handheld Mobile Devices. *ACM Comput. Surv.* **56**, 1–38 (2024).

Acknowledgments:

Funding: This work was supported by the National Natural Science Foundation (92580209, U25A6021, U20A20168) of China, the National Key R&D Program (2022YFB3204100), the Research Fund from Tsinghua University Initiative Scientific Research Program, a grant from the Guoqiang Institute, Tsinghua University, Scientific and Technological Innovation Project of China Academy of Chinese Medical Sciences (ZN2023A01, CI2023C002YG), China Institute for Rural Studies (CIRS2025-9), and Institute for Intelligent Healthcare, Tsinghua University.

Author contributions: T.-L.R., Y.Y. and L.-Q.T. directed and supervised the entire project. X.J. led the implementation of the study, developed the device, carried out comprehensive testing, and wrote the manuscript with input from all co-authors. X.J. and B.Z. were responsible for device testing, data collection, and image preparation. J.Y., H.L., and J.P. assisted in device fabrication and testing. T.-L.R., Y.Y. and L.-Q.T. provided leadership for project execution and manuscript preparation. All authors contributed to manuscript drafting and data interpretation.

Competing interests: Authors declare that they have no competing interests.

Data and materials availability: All data are available in the main text or the supplementary materials.

We thank Servier Medical Art, licensed under a Creative Commons Attribution 3.0 Generic License (http://smart.servier.com/; https://creativecommons.org/licenses/by/3.0/), for part of Supplementary Fig. 1.

Methods

Fabrication of Passive RF Chs

A 2 μm thick parylene film was deposited on a 2-inch silicon wafer using chemical vapor deposition (SCS Labcoter2, PDS 2010). Subsequently, a 200 nm thick Cu layer was sputtered on the surface as a seed layer for electroplating. The electroplating area was defined using standard photolithography with AZ12XT-10 photoresist. A Cu layer with the thickness of 5 μm was electroplated to form the passive RF Chs. PDMS (Sylgard 184, Dow Corning) was prepared by mixing the base and curing agent in a 10:1 weight ratio and stirring thoroughly. The mixture was then degassed in a plastic vacuum desiccator for 10 minutes to remove bubbles. The degassed PDMS was spin-coated at 1500 rpm for 60 seconds onto the silicon wafer to encapsulate the passive RF Chs and cured at 80° C for 1 hour. Finally, the encapsulated passive RF Chs were peeled off from the silicon wafer and cut into circles with diameters of 3 mm.

Fabrication of Embobi

For the embedded Embobi, After the micro pressure sensor was fabricated, it was placed with the coil side facing outward onto the convex surface of a dedicated contact lens mold. Due to the intrinsic smoothness of PDMS, the microsensor adhered naturally via van der Waals forces. The rigid gas-permeable lens material (20% HEMA, 75% FIPMA as monomers, 4% EGDMA as crosslinker, and 1% TPO as photoinitiator) was then poured into the mold and cured under 365 nm UV light for 1 min. After demolding and trimming, a complete embedded Embobi device was obtained. This process directly parallels the industrial fabrication of commercial contact lenses, ensuring good manufacturability. The device was then treated with oxygen plasma (100 W, 100 sccm, 1 min), followed by deposition of HEMA solution (with 1% EGDMA and 1% TPO) onto the cornea-facing surface. The device was placed face down, allowing gravity to induce natural leveling and infiltration of the solution. After a further 1 min of UV curing, a thin PHEMA coating was retained on the inner surface. The device was then immersed in PBS for 48 h to ensure full hydration of the hydrogel layer and removal of unreacted monomers. PHEMA is widely used in soft contact lenses, ensuring excellent compatibility with the cornea. Notably, the embedded Embobi substrate is composed of materials identical to those used in commercial RGP and contact lenses, ensuring both biocompatibility and commercial compatibility.

Cell Viability Test

The time-dependent viability of HCE-T cells exposed to Embobi was assessed following the ISO 10993-5 extraction protocol. Extracts were prepared by immersing the different samples into complete HCE-T medium at 37 °C for 24 h, with a sample-to-medium ratio of 0.2 g/mL. Three groups were evaluated: (1) complete culture medium (negative control), (2) Embobi extract (experimental group), and (3) 3–5% DMSO in complete culture medium (positive control). After several passages, HCE-T cells were seeded and subsequently incubated with the respective extracts for 24 h and 48 h. Cell viability was quantified using proliferation assays (n = 6 per group). In addition, we performed fluorescence live/dead staining using Calcein-AM/PI combined with Hoechst nuclear counterstaining, and obtained three-channel fluorescence images of the HCE-T cells under the same incubation conditions. Statistical analysis was performed using one-way ANOVA with Python to compare the experimental and positive control groups with the negative control group.

Gaze-written digit trajectory acquisition

The gaze-written digit experiments were performed using a programmable mechanical eye model to obtain controlled ocular trajectories and corresponding resonance responses. The mechanical eye consisted of an eyeball and eyelid structure mounted on a two-axis motorized platform. A smartphone-based control interface was used to drive two control parameters (X, Y), where X controlled horizontal rotation (left–right) and Y controlled vertical rotation (up–down). This established a one-to-one mapping between commanded (X, Y) coordinates and the eyeball's gaze orientation. During experiments, the reader coil was positioned in front of the smart contact lens at an approximate distance of 5 mm. A vector network analyzer continuously acquired the resonance spectra wirelessly, and the resonance-peak amplitudes of three channels were extracted in real time as multi-channel

temporal signals.Digit trajectories (2–9) were generated by driving the eyeball along predefined stroke paths in the (X, Y) coordinate space. The trajectories were executed either by manually dragging the gaze point in the control interface or by directly inputting serialized (X, Y) values to reproduce fixed motion patterns. Each trial produced synchronized three-channel resonance amplitude sequences corresponding to the digit-shaped gaze trajectory.

For comparative evaluation of gaze-direction tracking performance, eye-movement trajectories were simultaneously recorded using Embobi and a commercial infrared reflection–based eye tracker (Sol-glasses, Zhitung Huayu Co., Ltd.). The recorded trajectories were used to compare reconstruction accuracy and tracking characteristics between the two systems.

Directional tracking benchmark using a robotic eye

Directional tracking accuracy was evaluated using a programmable robotic eye platform. The eye motion was controlled through a mobile application, which generated predefined yaw–pitch trajectories corresponding to the letters “T”, “h”, and “U”. The control software provided the commanded angular positions with a resolution of 0.5°, which were used as the ground-truth reference for the robotic eye motion.

Trajectory reconstruction was performed using both Embobi and a commercial infrared reflection–based wearable eye tracker (Sol-glasses, Zhitong Huayu, nominal accuracy 0.5°). For both measurements, the same robotic eye model executed identical trajectories under the same control program. The reconstructed gaze trajectories from each system were then compared with the theoretical angular trajectories generated by the control software.

Directional accuracy was quantified by computing the angular differences between the reconstructed trajectories and the ground-truth trajectories along both the yaw and pitch axes. The distribution and standard deviation of these angular errors were used as the performance metrics.

Nine-key ocular input system

Gaze-based writing provides a feasible communication pathway for individuals with aphasia, anarthria, or severe motor impairments; however, letter-by-letter input is inherently inefficient and often induces visual fatigue while increasing recognition complexity. To address these limitations, we propose an interaction scheme that integrates temporal eye-movement tracking with a nine-key input framework. By replacing character-level spelling with gaze-written digits (2–9) and applying machine-learning–based classification of ocular trajectories, the system maps recognized digit sequences to candidate words within the nine-key paradigm. This approach enables word-level input without continuous visual fixation on a display, substantially improving input efficiency and reducing user burden. Using a lightweight two-dimensional convolutional neural network (CNN) for end-to-end trajectory classification, the system achieves a recognition accuracy of 96.4% on the validation dataset (Fig. 5D), with the learned embeddings exhibiting clear class separability in a low-dimensional feature space (Fig. 5C). In a practical demonstration, a biomimetic eye sequentially wrote the digits “4–6–6,” which were correctly recognized and decoded as the word “good” (see Supplementary Fig. xxxx and Supplementary Movie xxx for details).

VR-based spatial navigation platform

To evaluate the feasibility of Embobi for immersive spatial interaction, an eye-driven virtual reality (VR) navigation platform was developed. The system integrates three modules: (i) Embobi-based gaze sensing, (ii) real-time gaze decoding and classification, and (iii) VR scene control implemented in Unity.

During operation, resonance signals from the smart contact lens were continuously acquired using a reader coil connected to a portable vector network analyzer. Three-channel resonance amplitude features were extracted in real time and segmented into fixed temporal windows (50 frames per segment). Each segment was resampled to a uniform length (55 frames) to ensure temporal consistency for model input. The processed features were fed into a pretrained deep-learning classifier that output one of four canonical gaze directions (up, down, left, right). The forward direction was defined as the neutral baseline. The VR interaction module was implemented as a standalone executable program developed in Unity. After system initialization, the user’s gaze commands were

mapped to viewpoint control and navigation actions within a virtual indoor environment containing static objects such as furniture and walls. Predicted gaze directions were translated into smooth mouse-motion or keyboard-like control signals to emulate head rotation or forward/backward movement. A gradual motion update with a default step interval of 0.5 s was introduced to avoid abrupt transitions and reduce motion discomfort. In the VR navigation task, gaze direction determined steering orientation, while sustained fixation in a given direction triggered continuous movement along that heading. The system operated in a closed loop, with real-time gaze decoding driving dynamic viewpoint updates. All computations were performed on a local workstation without cloud processing, enabling lightweight, edge-level interaction.

Eye-controlled wheelchair navigation and occluded-target discrimination

To demonstrate real-world eye–machine interaction enabled by Embobi, we implemented a gaze-controlled wheelchair navigation system that integrates gaze-direction decoding with fixation-depth estimation. The overall control architecture is illustrated in Supplementary Fig. 16.

During operation, resonance spectra from the Embobi contact lens were continuously monitored on a computer via a NanoVNA interface. Direction-related amplitude features and curvature-related resonance-frequency shifts were extracted from the acquired spectra to decode gaze direction and fixation depth, respectively. Temporal window decoding was used to separate these two signals: gaze direction was estimated from the first 20 frames of the spectral sequence, while fixation depth was determined from the subsequent 20 frames.

The decoded gaze direction controlled the steering command of the wheelchair (left, right, or forward), whereas fixation depth determined the travel distance. Navigation experiments were conducted on a custom-built nine-grid floor map, in which each grid represented a discrete target location. Fixation corresponding to a near command triggered motion over one grid cell, while far fixation triggered motion over two grid cells in the selected direction.

For system integration, the computer performed spectral acquisition and gaze decoding from Embobi signals. The resulting navigation command (direction + distance) was transmitted via a USB connection to a smartphone, which relayed the command to the wheelchair through Bluetooth using a mobile control application. Wheelchair motion execution and trajectory progression were monitored visually during the experiments.

To evaluate the ability of depth-aware gaze sensing to resolve spatial ambiguity, an occluded-target discrimination experiment was performed in which targets shared similar viewing directions but differed in depth. In this scenario, a commercial eye tracker (Sol-glasses) was used as a baseline system for comparison with Embobi.

Water-lens eye model for curvature modulation

A biomimetic water-lens eye model was constructed to provide controllable corneal curvature modulation. The model consisted of a sealed plastic chamber (diameter 10 mm) enclosed by stretchable polyurethane membranes on both sides (membrane thickness $\approx$ 50 μm). A fluid inlet port was integrated into the side wall of the chamber to allow water injection. When liquid was introduced into the chamber, the polyurethane membranes expanded outward to form a dome-shaped surface whose curvature depended on the internal fluid volume. To ensure stable yet compliant contact between the device and the deformable membrane, the polyurethane surface was rendered mildly tacky using a thin pressure-sensitive adhesive layer. The Embobi contact lens was then gently placed on the membrane without rigid mechanical fixation, allowing the membrane to deform freely during curvature modulation.

The curvature radius of the water-lens surface was adjusted by controlling the injected water volume using a microfluidic pump connected to a syringe reservoir. During each experiment, the curvature radius was tuned to approximately 7 mm, corresponding to the typical range of human corneal curvature. Surface deformation was recorded from the side using a digital camera, and the surface contour was extracted using image-processing algorithms. The curvature radius was calculated by fitting the extracted contour to a circular arc using least-squares fitting.

For dynamic modulation experiments, the same fluidic system was used to vary the injected volume at controlled flow rates. Two modulation speeds were applied by setting the microfluidic pump to 1 mL min^{-1} and

2 mL min^{-1}, respectively, while maintaining a fixed injection volume of 0.05 mL per step. The Embobi smart contact lens was gently placed on the membrane surface during measurements, and its resonance response was continuously monitored through the wireless readout system.

Ex vivo porcine eye measurements

Fresh porcine eyeballs (n = 10) were obtained from a local abattoir shortly after slaughter. Prior to experiments, the eyeballs were visually inspected, and three specimens exhibiting clear corneas and regular anterior-surface morphology suitable for keratometer measurement were selected for testing. Each eyeball was fixed on a foam board using specimen pins to stabilize its orientation during measurements.

A 24-gauge intravenous catheter was inserted into the anterior chamber through the corneal limbus. The catheter was connected to a microsyringe pump (LSP02-2A, Longer Precision Pump) to inject saline into the eyeball, thereby modulating the corneal curvature by increasing intraocular volume.

The Embobi device was gently placed on the corneal surface of each eyeball during measurements. The position of the external reader coil was adjusted until stable resonance peaks were obtained and then fixed in place using a mechanical holder to prevent movement during experiments. In the relaxed ex vivo state, the porcine cornea typically exhibited a curvature radius of approximately 9 mm, slightly larger than that of the human cornea. Saline was gradually injected using the microsyringe pump to increase the internal volume of the eyeball, resulting in progressive corneal swelling and curvature change. Under these conditions the corneal curvature radius could typically be reduced to approximately 7 mm. The resonance-frequency response of the Embobi device and the corresponding corneal curvature radius were recorded simultaneously throughout this process.

The corneal curvature radius at the initial and final states was measured using a keratometer (SW-100, Suowei) to provide absolute calibration references. During injection, the central anterior corneal contour was continuously recorded using a side-view camera. In each frame, the contour was extracted by image processing and fitted to a circular arc using least-squares fitting. Pixel-to-length conversion was calibrated using a reference object placed in the imaging plane. The image-derived radius values were calibrated against the keratometer measurements to obtain the continuous curvature-radius trace used for analysis. Pixel-to-length conversion was calibrated using a reference ruler placed in the same imaging plane as the eyeball during imaging. The known scale markings on the ruler were used to determine the pixel-to-length conversion factor. The extracted corneal contour was then converted into physical coordinates and fitted to a circular arc using least-squares fitting to obtain the curvature radius.

To prevent dehydration of the ex vivo tissue during experiments, the exterior surface of the eyeball was periodically moistened with saline while avoiding direct liquid contact with the cornea or the sensing device, thereby maintaining tissue hydration without disturbing the resonance measurement.For the reproducibility test shown in Fig. 4G, three independently fabricated Embobi devices were sequentially tested on the same porcine eyeball to evaluate device-to-device consistency in curvature sensitivity.

In vivo rabbit experiments

Animals

Three adult New Zealand white rabbits (of either sex, body weight 2.5–3.0 kg) were used in this study. All procedures were conducted in accordance with institutional guidelines for animal care and were approved by the local Animal Ethics Committee. All procedures complied with the ARVO Statement for the Use of Animals in Ophthalmic and Vision Research.

Device wearing and ocular compatibility assessment

Embobi contact lenses were gently placed on the corneal surface of one eye of each rabbit, while the contralateral eye served as an untreated control. After device placement, a reader coil connected to a NanoVNA (NanoVNA-H4) was positioned near the eye for wireless resonance interrogation. The reader coil was fixed using a mechanical holder to maintain a stable relative position during measurements.

Rabbits were allowed to remain in their cages and perform normal daily activities during the monitoring period. Ocular surface temperature during operation was recorded using a macro infrared camera (HM-TPK20-3AQF/W, HIKMICRO). After 48 h of continuous wear, the Embobi lenses were removed and the corneas were examined using a slit-lamp microscope. The slit-lamp images were compared with baseline images acquired prior to device placement to evaluate possible corneal irritation or structural changes.

In vivo corneal curvature measurements

Corneal curvature sensing was evaluated under different natural body postures of the rabbits, including supine, 45° tilt, and 90° tilt positions. For each posture, the resonance spectrum of the Embobi device was recorded using the NanoVNA reader coil positioned near the eye.

Following each measurement, the corneal curvature radius was independently measured using a commercial keratometer (SW-100, Suowei) to provide reference values. Curvature measurements were obtained from three rabbits under the different postural conditions to generate multiple calibration points for the frequency–curvature relationship.

To extend the measurable curvature range, additional curvature modulation was induced in one rabbit by controlled saline infusion into the anterior chamber. Under intramuscular anesthesia, an infusion needle was inserted into the anterior chamber through the corneal limbus. Saline was allowed to enter the eye by elevating the saline bottle relative to the anterior chamber, thereby increasing intraocular volume and producing a gradual increase in corneal curvature. Resonance spectra and corresponding keratometer measurements were recorded during this process.

All curve fitting and linear regression analyses were performed using Microsoft Excel.

In vivo eye-movement monitoring

Eye-movement monitoring was performed in awake rabbits. The rabbits were placed in a cage with their body posture stabilized, and the Embobi lens was positioned on the corneal surface. The reader coil was fixed near the eye using a mechanical holder to maintain stable wireless coupling.

Resonance amplitude signals from the multiple sensing channels were continuously recorded while the rabbits exhibited spontaneous eye movements under natural conditions. The recorded signals were used to reconstruct eye-rotation trajectories for yaw and pitch analysis.

Supplementary Files

This is a list of supplementary files associated with this preprint. Click to download.

- SupplementaryVideo1.mp4
- SupplementaryVideo2.mp4
- SupplementaryVideo3.mp4
- SupplementaryVideo4.mp4
- SupplementaryVideo5.mp4
- SupplementaryInformation.pdf